Research Article

Optimizing phase formation of $BiFeO_3$ and Mn-doped $BiFeO_3$ nanoceramics via thermal treatment using citrate precursor method

Waseem Ahmad Wani[1] · Souvik Kundu[2] · Kannan Ramaswamy[1] · B. Harihara Venkataraman[1]

Received: 17 May 2020 / Accepted: 12 October 2020 / Published online: 9 November 2020

Abstract
In recent years, bandgap tailoring of ferroelectric materials has gained great attention in the scientific community owing to their favourable materials characteristics, and new endowing paths for developing multifunctional devices. In this study, an attempt was made to tune the optical bandgap of $BiFeO_3$ (BFO) via chemical substitution and by controlling thermal treatment temperature and time. A series of $BiFe_{1-x}Mn_xO_3$ (x = 0.00, 0.03, 0.05) nanoceramic samples were prepared by adopting the citrate precursor method. The effect of Mn substitution, annealing temperature, and annealing time on structural, morphological, and optical properties of BFO was investigated using X-ray diffraction, field emission scanning electron microscopy, and UV–visible spectroscopy, respectively. The average crystallite size was found to decrease (from 44–17 nm) with Mn-doping and increase with increasing annealing temperature and time (from 17–27 nm) due to the agglomeration of nanoparticles. The FESEM studies revealed the inhomogeneous distribution of granular structured grains with negligible porosity. The optical bandgap energy of BFO nanoparticles was found to reduce significantly by 21% (2.08–1.62 eV) with a competing effect of Mn-substitution, annealing temperature, and annealing time. The optical bandgap studies of $BiFe_{0.97}Mn_{0.03}O_3$ showed a direct correlation with annealing temperature and an inverse correlation with annealing time. Additionally, $BiFe_{0.97}Mn_{0.03}O_3$ nanoparticles annealed at 550 °C for 2 h showed a 31% enhancement in absorption coefficient and 14% reduction in bandgap value without a structural phase transition. The results obtained in this study propose $BiFe_{0.97}Mn_{0.03}O_3$ nanoparticles as a potential candidate for upcoming ferroelectric photovoltaic devices.

Keywords Multiferroics · Photovoltaics · Bismuth ferrite · Optical properties

1 Introduction

Recently, multiferroic materials that exhibit multiple ferroic orders simultaneously have gained widespread applications in spintronics, information storage, sensors, actuators, and photovoltaic devices [1–4]. Amongst the several multiferroic materials, $BiFeO_3$ (BFO) is probably the only lead-free multiferroic material showing room temperature ferroelectric and G-type anti-ferromagnetic orders simultaneously. Rhombohedrally distorted perovskite (ABO_3) structured BFO, with R3c space group shows high anti-ferromagnetic Neel temperature, ($T_N \sim 370$ °C) and high ferroelectric temperature ($T_C \sim 830$ °C) [5, 6]. The anti-ferromagnetic nature in BFO arises due to partially filled d-orbitals of Fe^{3+} at B site, and ferroelectric order develops due to the presence of $6s^2$ lone pair of electrons of Bi^{3+}at A site [7]. Owing to its unique features such as large remnant polarization (90μC/cm^2) and relatively lower bandgap (2.08–2.7 eV) compared to other oxide-based

✉ B. Harihara Venkataraman, hari@hyderabad.bits-pilani.ac.in | [1]Department of Physics, Birla Institute of Technology and Science (BITS) - Pilani, Hyderabad Campus, Hyderabad 500078, India. [2]Department of Electrical and Electronics Engineering, Birla Institute of Technology and Science (BITS) - Pilani, Hyderabad Campus, Hyderabad 500078, India.

ferroelectrics, BFO is considered as one of the emerging ferroelectric photovoltaic materials [4].

Additionally, this material shows above bandgap photovoltage and bulk based photovoltaic effect due to the polarization-based charge transport mechanism. Therefore there is a possibility to implement this advantage to higher photovoltaic efficiency if the short circuit current density can also be augmented. Despite these intriguing physical properties, BFO suffers from some significant limitations like large leakage current density and complex phase formation due to the volatile nature of bismuth. These factors restrict its applicability to device fabrication. Meanwhile, several attempts have been made to overcome these obstacles which include doping at Bi-site with rare-earth ions (Y, Pr, Ho, Eu, Gd, Sm, etc.) [8–13] and doping at Fe-site with transition metal ions (Co, Cr, Mn, Ni, etc.) [14, 15]. Doping at A site with rare-earth elements controls bismuth volatility and hence suppresses the generation of oxygen vacancies while doping at B site with donor elements fills the oxygen vacancies, and therefore reduces the leakage current.

Furthermore, most of these attempts have proved beneficial in modifying various other parameters, such as dielectric constant, resistivity, magneto-electric coupling, and optical bandgap values. Mn-substitution at Fe site in BFO is attractive, owing to its excellent chemical stability (in terms of oxidation state), comparable size, and its tendency to modify optical bandgap. Zhu et al. tailored the optical band gap of BFO with co-doping of Eu and Mn atoms in BFO from 2.40–1.49 eV [16]. Chandel et al. reported enhanced electrical and magnetic properties in Mn-doped BFO nanoparticles [22]. Hiroshi et al. investigated the impact of annealing temperature on Mn-doped BFO films [6]. The effect of Mn-doping concentration on the multiferroicity of BFO was investigated by Chauhan et al. [5]. Irfan et al. tailored the optical bandgap of BFO from 2.08–1.45 eV via chemical substitution of Sm and Mn at Bi and Fe sites of BFO [13]. So far, no investigations exist to understand the influence of annealing time and annealing temperature on the optical properties of BFO.

Synthesis of pure phase BFO is a challenging task because of the volatile nature of bismuth, and the kinetics of formation. Various methods have been adopted so far, to prepare pure phase BFO, which include solid-state reaction method [17], liquid phase sintering [18], citrate precursor method [19, 22], the hydrothermal method [20], and sol–gel method [14]. Most of these methods require high annealing temperature (usually more than 650 °C), thus yielding one or the other undesirable secondary phases along with pure phase BFO due to the volatile nature of bismuth. Several research groups have used an excessive amount of Bi (between 3–10 mol%) to prevent undesirable effects arising from the volatility of Bi [11, 21]. At the same time, some others are doing post-annealing nitric acid treatment to purify the samples [17]. Thus, the impact of thermal annealing treatment (annealing temperature and annealing time) on the synthesis of BFO appears to be a suitable method to reduce/eliminate the occurrence of secondary phases in BFO. Furthermore, among the several synthesis routes mentioned above, the citrate precursor method seems to be one of the potential alternatives for synthesizing nanoparticles, as this allows reasonable control of the stoichiometry. Moreover, this method is carried out at a relatively low temperature (600 °C) and also a cost-effective process with simple processing steps. The steps involved in this process are mixing, gelation, drying, and sintering, and hence this method does not require complicated or expensive instrumentation.

As far as our knowledge is concerned, several research groups have synthesized single-phase BFO by adopting advanced techniques or by post leaching treatment. However, by adopting the citrate precursor method, it is very difficult to obtain a pure/primary-phase of undoped and Mn-doped BFO nanoparticles at low temperatures (550 °C). Most of the reported methods have (1) lead to the formation of secondary phases, (2) used excessive bismuth content, or (3) adopted post-annealing nitric acid treatment for purification. Therefore, in this study, we report the phase formation of undoped BFO and Mn-doped BFO (with a negligible trace of impurity phase) using citrate precursor method at lower temperature (550 °C) by optimizing annealing temperature and annealing time. After that, we systematically varied annealing temperature (from 500 °C to 600 °C) and annealing time (from 2–6 h) of different series of samples and carefully investigated their effects on structural, morphological, and optical properties. The results showed a significant variation in the optical bandgap of Mn-doped BFO with annealing temperature and annealing time. The optical bandgap of BFO was reduced to 1.62 eV by tuning Mn-doping, annealing temperature, and annealing time.

2 Experimental details

2.1 Preparation

In the current study, single-phase undoped BFO, and Mn-doped nanoparticles were prepared by adopting the citrate precursor method. The precursors taken in the synthesis process were bismuth nitrate pentahydrate ($Bi(NO_3)_3.5H_2O$), iron nitrate nonahydrate ($Fe(NO_3)_3.9H_2O$), manganese acetate dihydrate ($C_6H_9M_nO_6.2H_2O$), citric acid ($C_6H_8O_7$), and diluted nitric acid (HNO_3). All the reagents were purchased from Sisco Research Laboratories (SRL) Pvt. Ltd. India and were used

without further purifications owing to their high purity analytical grades. In the first step, stoichiometric proportions of bismuth nitrate pentahydrate, iron nitrate nonahydrate, and manganese acetate were dissolved in the distilled water solvent at room temperature. Citric acid, which is a chelating agent, was added to the metal nitrate solution with citric acid to metal cation molar ratio of 2:1. Secondly, diluted nitric acid was added drop-wise to the light-yellow coloured mixture at constant stirring until a homogeneous sol was obtained. The resultant precursor sol was heated at 80 °C under vigorous stirring using a magnetic stirrer to procure gel-deposit. Immediately after the gelation process, the gel-deposit was dried at 130 °C for about 6 h to get a fluffy residue. Finally, the flocculent residue was ground using the pestle and mortar to extract fine powder. The as-obtained fine powder was calcined under controlled thermal treatments ranging from 350–450 °C to optimize the calcination temperature, which was later found to be 400 °C. Subsequently, the calcined powder (at 400 °C) was ground again and pelletized into cylindrically shaped pellets with a 10 mm diameter of varying thickness. In the end, the obtained pellets were annealed at different temperatures (500 °C, 550 °C, and 600 °C) for different durations (2 , 4 , and 6 h) to optimize the single-phase formation of undoped and Mn-doped BFO. The heating rate (4 °C/minute) was maintained constant at all the stages of this process. Undoped BFO was prepared using the same procedure without adding manganese acetate dehydrates. The flow chart describing the present synthesis method is depicted in Fig. 1.

2.2 Characterization

X-ray diffraction (XRD) studies were carried out to determine the crystal structure of the prepared compounds using X-ray diffractometer (Rigaku Ultima-IV XRD) with CuKα (λ = 1.5406 Å) radiation source with step size 0.02° in the 2θ range from 20°–70°. Field emission scanning electron microscope (FEI- Apero LoVac FESEM) (accelerating voltage 20 kV) assembled with energy-dispersive X-ray spectroscopy (EDAX) was used to investigate the morphological and compositional features of all the samples. Fourier transform infrared (JASCO FT/IR-4200) spectral studies were carried out to investigate the stretching and bending behaviour of distinct bonds existent in the samples. Optical absorption spectral analysis of the samples was carried out using a UV–vis spectrophotometer (JASCO V—670), and the bandgap was calculated using Tauc's relation.

3 Results and discussions

3.1 Structural properties

3.1.1 Effect of annealing temperature on BFO

The phase formation and crystal structures of all the samples, annealed at different temperatures, and times were determined by XRD studies. Figure 2a shows the XRD patterns of undoped BFO nanoceramics calcined at different temperatures (350 °C, 400 °C, and 450 °C). The XRD patterns of the samples calcined at lower

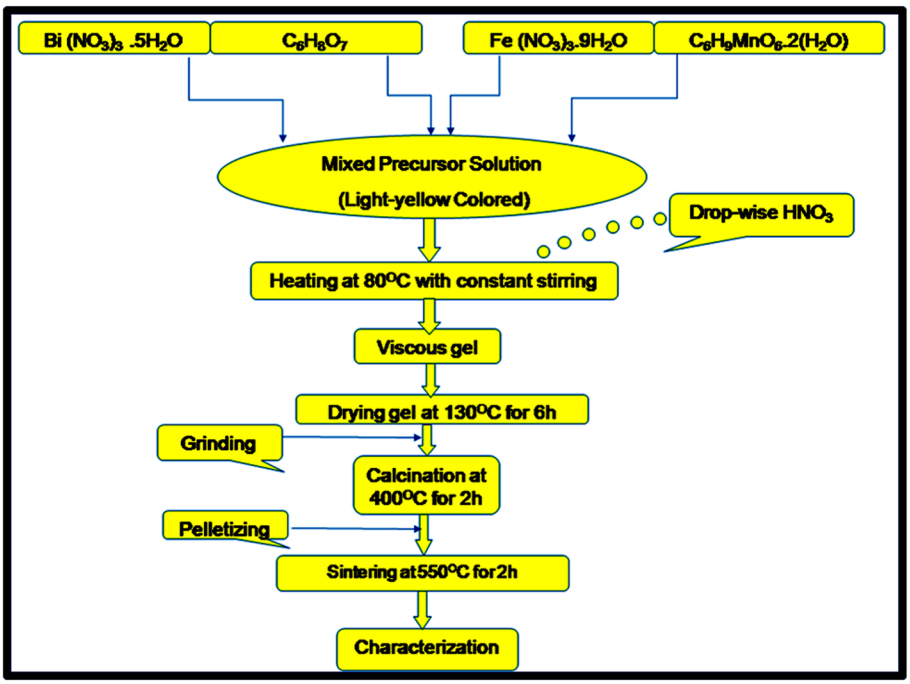

Fig. 1 Synthesis procedure

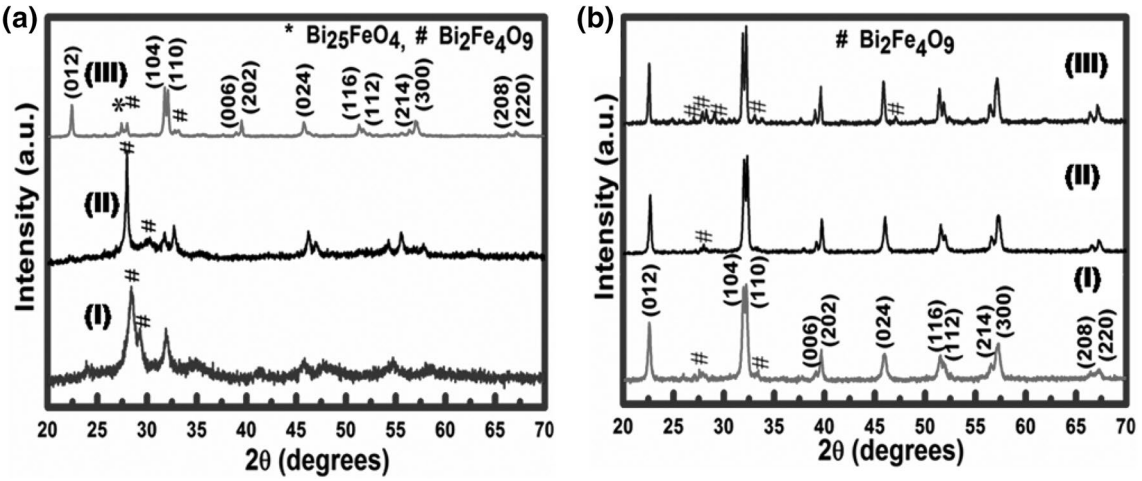

Fig. 2 XRD pattern of **a** BFO calcined at (I) 350 °C, (II) 400 °C, (III) 450 °C, **b** BFO calcined at 400 °C and annealed at (I) 500 °C, (II) 550 °C, (III) 600 °C

temperatures (350 °C, 400 °C, and 450 °C) showed only a few Bragg peaks depicting the weak crystalline nature along with some secondary phases. To enhance the crystalline quality of the prepared samples, these were annealed at higher temperatures. Figure 2bdepicts the XRD patterns of the undoped BFO samples calcined at 400 °C and annealed at 500 °C, 550 °C, and 600 °C. The XRD peaks of these samples reveal that both the crystallinity and phase purity of samples improved significantly with increasing annealing temperature. Furthermore, the XRD pattern of the sample annealed at 550 °C confirmed the phase formation of BFO with a negligible trace of impurity phase having rhombohedrally distorted perovskite structure, and R3c space group [21]. These results are in agreement with the JCPDS data file (PDF#861,518). However, the samples annealed at 500 °C and 600 °C showed few secondary peaks of $Bi_2Fe_4O_9$ in the XRD pattern, which might be due to kinetics of formation, and volatile nature of bismuth [21].

3.1.2 3.1.2 Effect of Mn-doping on BFO

Figure 3a shows the XRD patterns of $BiFe_{1-x}Mn_xO_3$ (x = 0.0, 0.03, 0.05) (BFMO) calcined at 400 °C for 2 h and annealed at 550 °C for 2 h. All the Bragg's peaks confirmed the formation of a single-phase of Mn-doped BFO. However, a minute trace of the secondary phase ($Bi_2Fe_4O_9$) was also detected, which was found to decrease with an increase in Mn-concentration. However, for 5 mol% Mn-doped sample, the $Bi_2Fe_4O_9$ disappeared completely, and a new impurity phase of $Bi_{36}Fe_2O_{57}$ appeared in the XRD pattern, as shown in Fig. 3a. As seen in Fig. 3a, the (110) and (104) planes start merging into a single peak with Mn-doping and finally appears as a single peak at 5 mol% doping

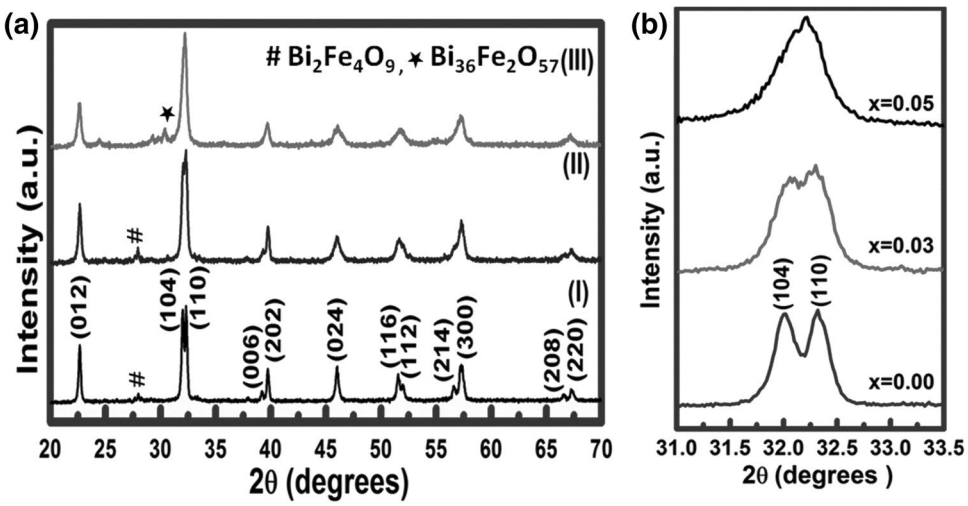

Fig. 3 **a** XRD pattern of $BiFe_{1-x}Mn_xO_3$ compositions calcined at 400 °C and annealed at 550 °C with (I) x = 0.00, (II) x = 0.03, (III) x = 0.05 **b** Magnified view of $BiFe_{1-x}Mn_xO_3$

concentration. The merging of twin peaks suggests lattice distortion owing to the difference in ionic radii of the dopant and host ions, which results

in structural distortion with Mn-substitution [21, 22]. Moreover, the magnified view of the XRD patterns (Fig. 3b) clearly shows the overlapping of the peaks and the shifting of peaks towards higher 2θ values with Mn-doping which can be ascribed to size difference in the ionic radii of Fe^{2+} (0.782 Å) and Mn^{3+} (0.645 Å) ions. The obtained results were found to be in line with the studies carried out by Chandel et al.[22] and Hua et al. [23]. Therefore, one can notice that Mn-substitution in Fe site is an effective way to modulate the crystal structure of BFO. Thus, 3 mol% Mn-doping in BFO is considered to be the optimum doping concentration for tailoring the optical parameters.

3.1.3 Effect of Annealing Temperature on Mn-doped BFO

Next, to investigate the effect of annealing temperature on Mn-doped BFO, these samples were annealed at different temperatures. Figure 4 depicts the XRD patterns of BFMO (3 mol %) samples annealed at different temperatures (500 °C, 550 °C, and 600 °C) for 2 h. It is evident from these XRD patterns that all the BFMO samples annealed at different temperatures exhibit a rhombohedrally distorted perovskite structure. Moreover, the intensity of impurity peaks of these samples first reduced with increasing annealing temperature from 500 °C to 550 °C. Subsequently, the impurity peaks increased for the sample annealed at 600 °C. These results suggest that annealing temperature plays a decisive role in the pure phase formation of BFMO nanoparticles. Hence, annealing at 550 °C was found to exhibit the phase formation of BFO with a negligible trace of impurity phase and better crystallinity as compared to other BFMO samples annealed at different temperatures.

3.2 Effect of Annealing Time on Mn-doped BFO

Furthermore, to investigate the efficacy of annealing time on Mn-doped samples, the samples were annealed at 550 °C for different durations. Figure 5 shows the XRD patterns of these BFMO (3 mol %) samples annealed at 550 °C for 2 h, 4 h, and 6 h. All the samples exhibited good crystallinity, indicating the formation of perovskite structured material. However, the secondary phase formation was found to increase with increasing annealing time, which could be accounted for the excessive number of oxygen vacancies at higher dwell times or the creation of bismuth vacancies due to the volatile nature of bismuth. In addition to this, the peak widths at half maxima were found to decrease with an increase in annealing temperature, indicating variation in particle size. Thus, annealing temperature and time provide another tool to modulate the particle size, which in turn alters the physical properties.

Moreover, to correlate crystallite size with Mn-doping, annealing time, and annealing temperature, the average crystallite size was assessed from peak widths at half maximum of all the samples, using Debye–Scherrer formula

$$D = \frac{k\lambda}{\beta \cos\theta}$$

where D is crystallite size, k is the shape factor (~ 0.9), β is full width at half maxima (radians), λ is the wavelength of Cu K_{α}, and θ is diffraction angle. It was found that the average crystallite size decreased from 44–17 nm with increasing Mn concentration owing to the smaller ionic radius of Mn^{3+} (0.0645 Å) ion compared to the host site, Fe^{2+} (0.782 Å) ion. This result validates the substitution of Mn in the Fe site inside the host matrix. In addition to this, the average particle size was found to increase with

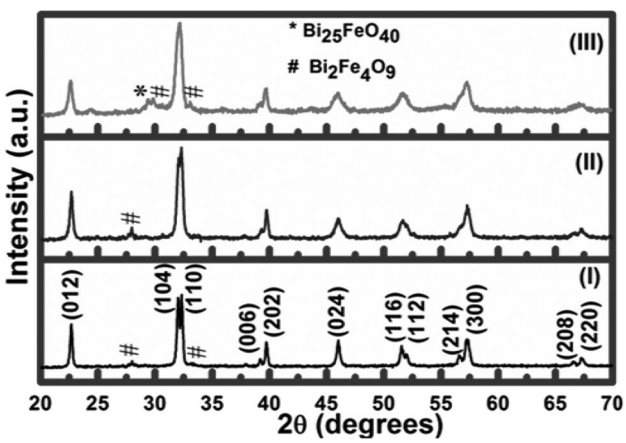

Fig. 4 XRD pattern of BFMO calcined at 400 °C and annealed at (I) 500 °C, (II) 550 °C, (III) 600 °C

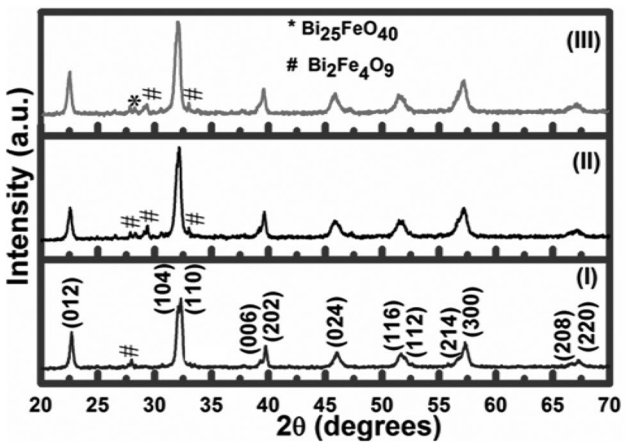

Fig. 5 XRD pattern of BFMO calcined at 400 °C and annealed at 550 °C for (I) 2 h, (II) 4 h, (III) 6 h

an increase in annealing temperature and annealing time for both undoped as well as Mn-doped samples. The average crystallite sizes of all the samples are summarized in Table 1.

3.3 Morphological properties

Figure 6a,b shows the micrographs of BFO and BFMO samples annealed at 550 °C for 2 h. As evident from these micrographs, the microstructures are evolving into more (or) less uniform granular structures with negligible porosity, and also, a gradual reduction in granular size with Mn doping is detectable. This result is in good agreement with XRD studies. Furthermore, the results showed a continuous grain growth in the BFO sample, whereas Mn-doped samples seem to experience discontinuous grain growth in some regions. The above analysis revealed that Mn doping inhibits grain growth, which might be due to different diffusion rates of metal ions.

Figure 7a–c show the FESEM images of BFMO samples annealed at different temperatures (500 °C, 550 °C, 600 °C) respectively. The specimen consists of small clusters of

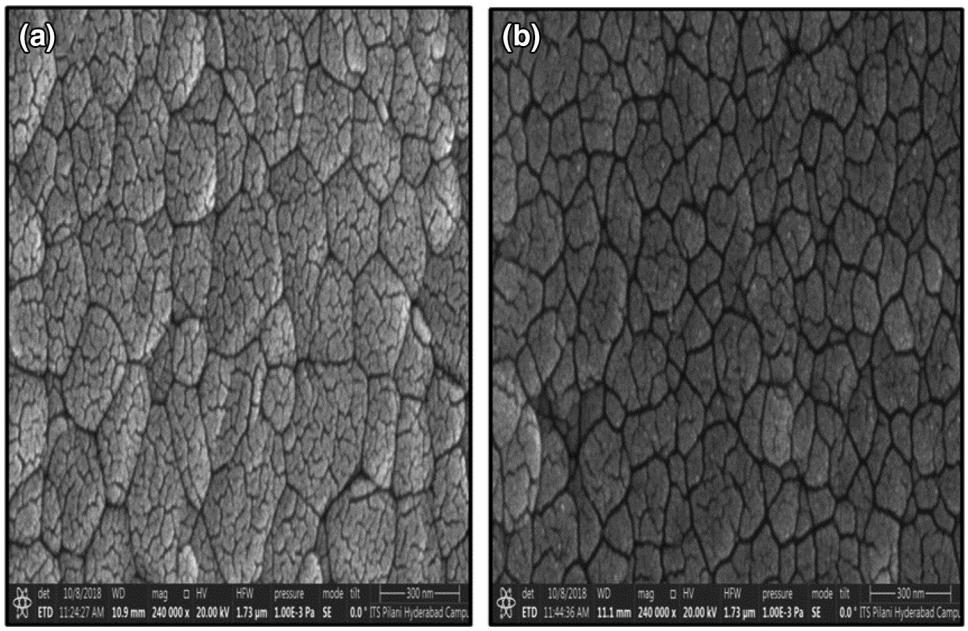

Fig. 6 **a** FESEM micrograph of BFO calcined at 400 °C and annealed at 550 °C for 2 h **b** FESEM micrograph of BFMO calcined at 400 °C and annealed at 550 °C for 2 h

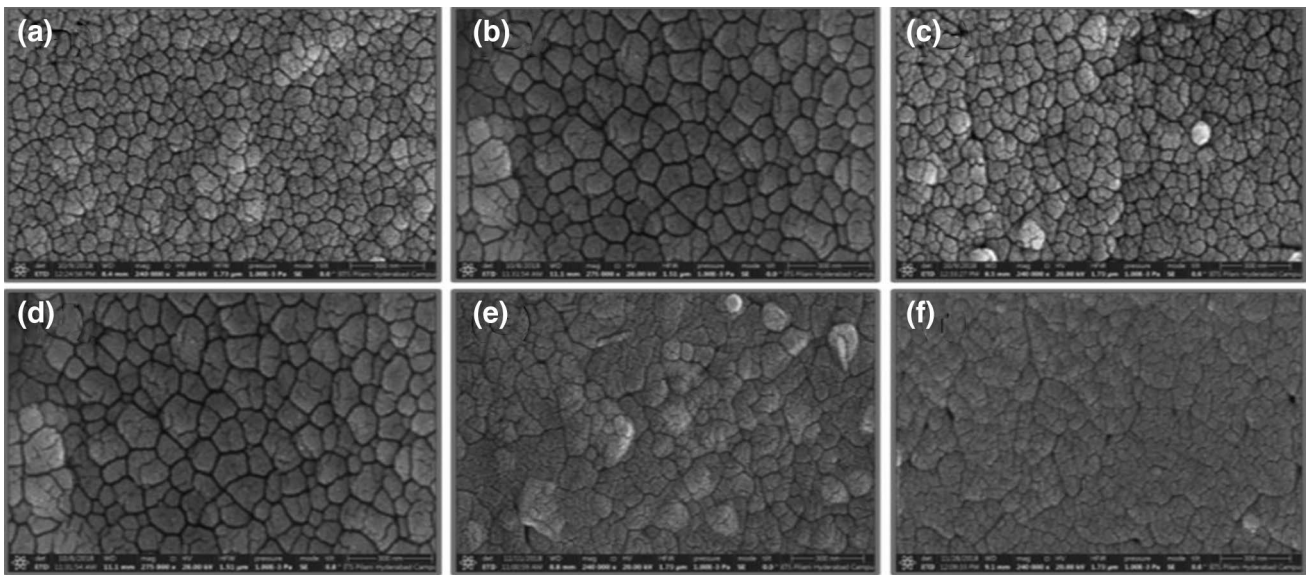

Fig. 7 FESEM micrograph of BFMO annealed at **a** 500 °C/2 h, **b** 550 °C/2 h, **c** 600 °C/2 h, **d** 550 °C/2 h, **e** 550 °C/4 h, **f** 550 °C/6 h

particles at lower annealing temperatures. As the annealing temperature was increased, the grain size was found to increase. Fig 7d–f depict the SEM images of BFMO samples annealed at 550 °C for different time durations (2 h, 4 h, and 6 h), respectively. It appears from these micrographs that granular size increases upon increasing annealing time and the samples become more agglomerated for higher annealing times.

3.4 Compositional properties

Energy-dispersive X-ray spectral studies were carried out to check the chemical composition of both the undoped BFO and BFMO samples, and the recorded spectra are shown in Fig. 8a and Fig. 8b, respectively. The analysis of these spectral patterns confirmed the presence of Mn in the doped sample, and also ruled out the presence of foreign elements in all the samples. In addition to this, the results obtained also gave a quantitative composition of all the constituents. The elemental concentration in terms of the atomic percentage of bismuth, iron, and oxygen in the undoped sample was found to be 20.34%, 22.73%, and 56.93%, respectively. In BFMO, the percentages of bismuth, iron, manganese, and oxygen are 20.29%, 19.67%, 2.36%, and 57.68%, respectively.

3.5 Elemental mapping studies

To confirm the uniformity of dopant (Mn) across the regions in the sample, elemental mapping images were recorded for the BFMO sample. Figure 8c–g show the images obtained from elemental mapping studies. Figure 8c, d, e show a uniform notation in the colour codes of Bi, Fe, and Mn, respectively, which indicates the homogeneous distribution of the elements in the BFO matrix. However, a non-uniform spread of the colour in Fig. 8f shows an irregular variation of oxygen content in the BFO matrix. The dark patches in Fig. 8f indicates the oxygen vacant regions. The mixed mapping image of all the constituent elements is shown in Fig. 8g. Thus, the elemental mapping analysis confirms the homogeneous distribution of the dopant ions in the BFO matrix. These results suggest that the citrate precursor preparation technique facilitates the uniform distribution of dopants in the BFO matrix.

3.6 3.5 FTIR studies

Figure 9 shows the FTIR spectra of undoped BFO and BFMO samples recorded in the wavenumber range 450–2000 cm^{-1}. FTIR spectral analysis is a crucial characterization tool that gives the qualitative as well as quantitative information about the sample by identifying the

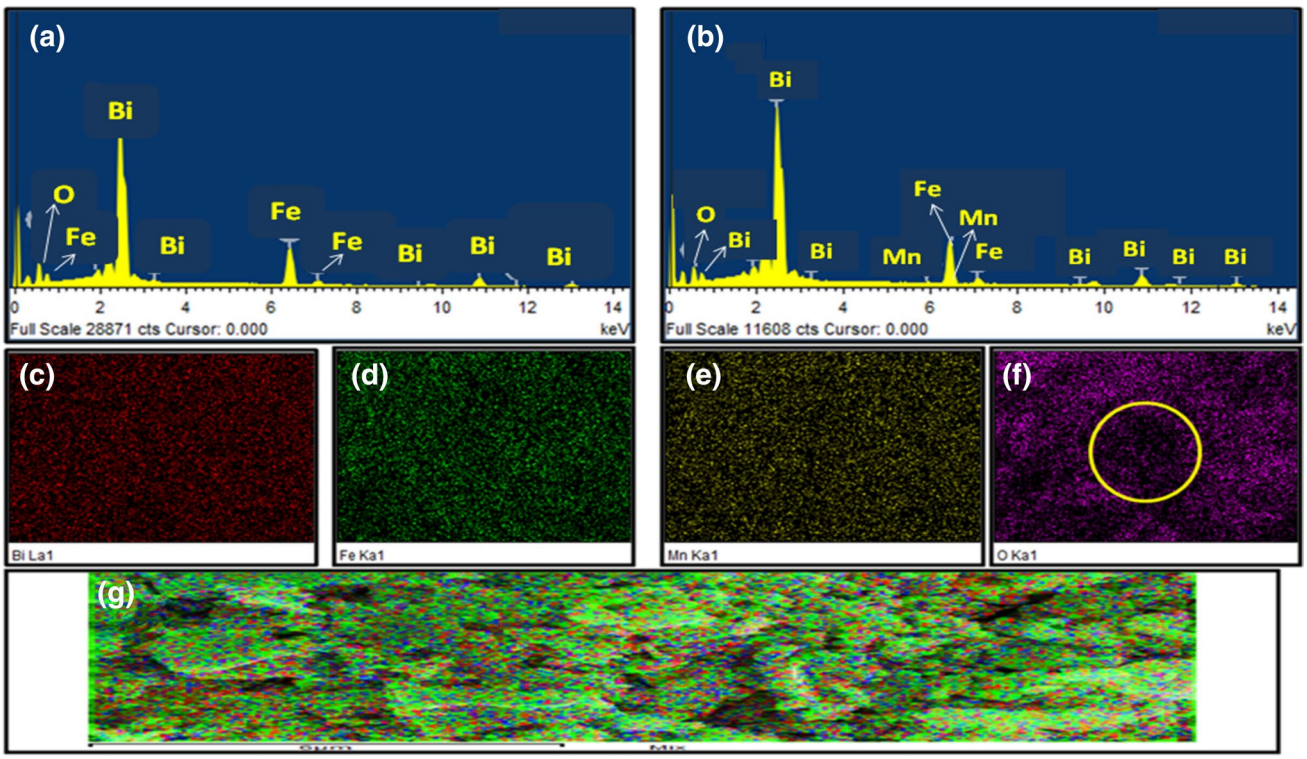

Fig. 8 EDAX spectra of **a** BFO, **b** BFMO, Elemental mapping images of constituent elements in BFMO **c** Bi, **d** Fe, **e** Mn, **f** O, **g** all constituents mixed

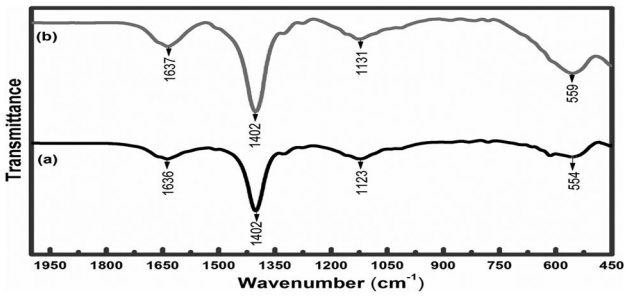

Fig. 9 FTIR spectra of **a** BFO, **b** BFMO

Table 1 Average crystallite size of undoped and Mn-doped samples under different conditions of thermal treatment

Composition	Mn Mol % (x)	Annealing temperature (°C)	Annealing time (hour)	Average crystallite size (nm)
$BiFe_{1-x}Mn_xO_3$	0	550	2	44
$BiFe_{1-x}Mn_xO_3$	3	550	2	24
$BiFe_{1-x}Mn_xO_3$	5	550	2	17
$BiFe_{1-x}Mn_xO_3$	3	550	4	26
$BiFe_{1-x}Mn_xO_3$	3	550	6	27
$BiFe_{1-x}Mn_xO_3$	3	500	2	18
$BiFe_{1-x}Mn_xO_3$	3	600	2	27

Table 2 Absorption bands of BFO and BFMO samples

Composition	Vibrational bands in cm^{-1}			
	V1	V2	V3	V4
BFO	554	1123	1401	1636
BFMO	559	1131	1402	1437

chemical bonds present in the sample. The sharp peaks in the band range 450–600 cm^{-1} are attributed to Fe–O stretching vibration and O–Fe–O bending vibration of the octahedral FeO_6 group. This result confirms the perovskite structure of our samples and is consistent, as reported by Liu et al. [24]. The peak at 1636 cm^{-1} is due to the bending vibration of O–H–O present in the sample, which might have incorporated during the synthesis process [8]. The bands observed around 1400 cm^{-1} and 1150 cm^{-1} are attributed to the trapped nitrates in the xerogel matrix during the synthesis process [8, 24]. Moreover, in the present work, it was observed that the strong absorption band (metal–oxygen band) shifted towards higher wavenumber with Mn-doping, which might be attributed to distortion occurring in the bonds due to difference in ionic radii. The positions of all obtained absorption bands are given in Table 2.

3.7 Optical properties

In order to study the optical properties of undoped BFO and BFMO samples under different thermal annealing conditions, the absorption spectra of all the samples were recorded in the wavelength range of 350–750 nm using a UV–visible photo-spectrometer. Figure 10a shows the strong absorption of undoped and Mn-doped samples in the visible region. A significant increase in absorbance was noticed with Mn-doping. Mn-substitution seems to be effectively absorbing more light in the wavelength range 500–750 nm. Absorption of light in the longer wavelength signifies narrowing energy absorption edge, which suggests a reduction in optical bandgap.

To quantify this fact, the absorption coefficient (α) of undoped and Mn-doped samples was calculated at 375 nm. The absorption coefficient was found to increase

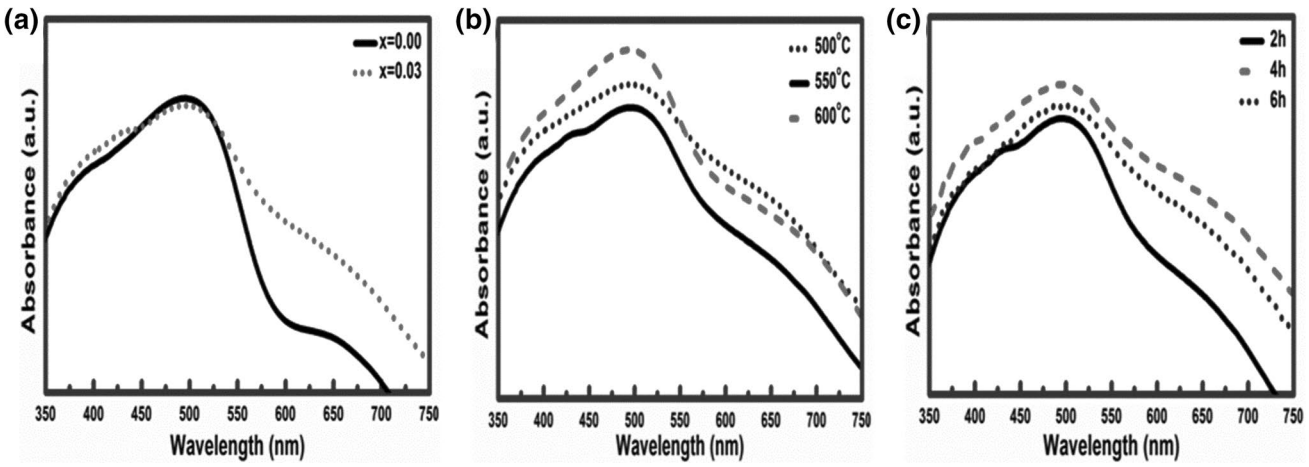

Fig. 10 Absorbance spectra of **a** $BiFe_{1-x}Mn_xO_3$ compositions **b** BFMO annealed at different temperatures for 2 h, **c** BFMO annealed at 550 °C for different durations

by 31% in comparison to BFO. These results predict that Mn-substitution in BFO may augment the light-harvesting efficiency (LHE) of the BFO matrix. The absorption coefficient was calculated using the relation

$$\alpha = 2.303\frac{(\mathrm{Ab})}{t}$$

where α is the absorption coefficient, (Ab) is absorbance, and *t* is the thickness of the sample [26]. To describe the relation between optical bandgap, and thermal treatment conditions of BFMO samples, the absorption spectra of all the samples with different annealing temperatures, and various heat dwell times were recorded and are shown in Figs. 10b,c, respectively.

The optical bandgap values of all the samples are calculated using Tauc's relation as given below [26, 27].

$$\alpha = \frac{C\left(h\upsilon - E_g\right)^{\frac{n}{2}}}{h\upsilon}$$

where *C* is parameter independent of the incident light, hυis the energy of incident light, α is absorption coefficient, *n* is a number equal to 4 for indirect semiconductors, and 1 for direct semiconductors. The bandgap values are calculated by plotting the dependence of $(\alpha h\upsilon)^2$ on incident light hυ and establishing linear extrapolation of $(\alpha h\upsilon)^2$ to zero while considering BFO as direct bandgap semiconductor material at room temperature.

Figure 11a shows the Tauc's plots for calculating the bandgap values of undoped BFO and BFMO samples. The direct bandgap value of BFO was found to be 2.08 eV, which is consistent with several reports addresses in literature [28–30]. Recently, Rhaman et al. (2019) reported a significant bandgap reduction in orthorhombic BFO via Co substitution [31]. To our interest, a considerable decrease in bandgap value from 2.08–1.79 eV was observed in the BFMO sample. There are several possibilities for this reduction in the bandgap values. One option speculates the fact that impurity levels are probably generated within the forbidden band, which may either shift the donor level over the actual valence band or acceptor level under the real conduction band and hence reduce the bandgap of Mn-doped sample. Lee et al. reported the optical band of $BiMnO_3$ to be 1.2 eV [32]. The other possible reason could be ascribed to rearrangement in molecular orbitals, and distortion generation in FeO_6 octahedral owing to the differences in ionic radii of Mn^{3+} and Fe^{3+} ions because the bandgap in BFO is measured between the Fe (3d) conduction band and mixed-valence band of O(2p)—Fe(3d) [33]. The variation in bandgap values of BFMO samples, annealed at 550 °C with different heat dwell times (2 h, 4 h, and 6 h), is shown in Fig. 11b. Lowest bandgap (1.62 eV) was observed for the sample with the most prolonged heat treatment time (6 h). Various parameters that may influence the bandgap include particle size, microstructural defects, chemical structure, and oxygen vacancies [34–37]. This reduction in bandgap values with increasing annealing time may be ascribed to an increase in particle size due to quantum size confinement [38].

Additionally, the XRD patterns clearly revealed the presence of the secondary phase of $Bi_2Fe_4O_9$ for the samples annealed for longer durations (4 h, 6 h), which is a low bandgap material with bandgap values ranging from 1.6–1.9 eV [39]. Thus, the presence of the secondary phase of $Bi_2Fe_4O_9$ poses another possible mechanism for bandgap reduction. The variation in optical bandgap values of BFMO samples with increasing annealing temperature is shown in Fig. 11c. The figure shows that the bandgap increases from 1.68–1.89 eV with an increase in annealing temperature. As XRD and SEM observations have shown an increasing trend in particle size with increasing annealing temperature, a reduction in bandgap values is expected.

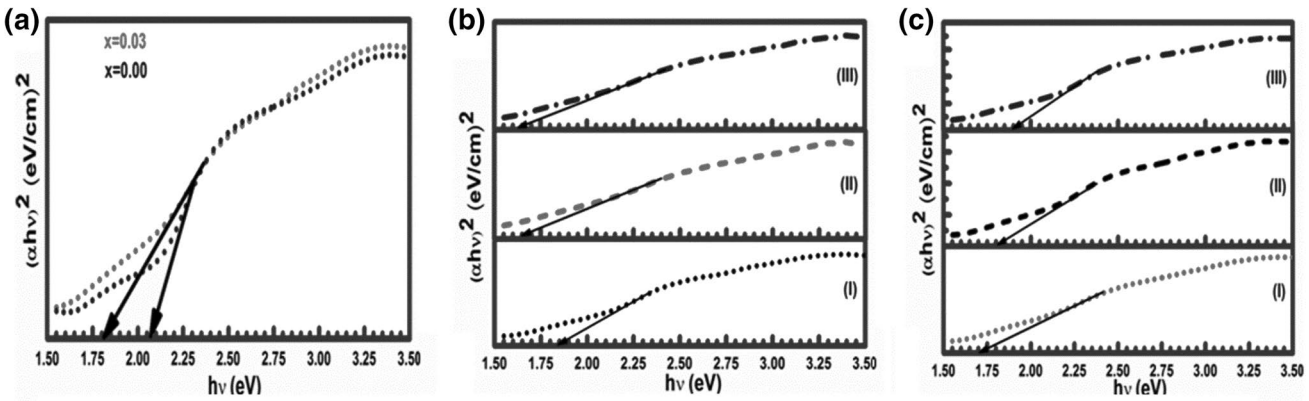

Fig. 11 $(\alpha h\upsilon)^2$ plotted as a function of hυ for **a** $BiFe_{1-x}Mn_xO_3$ compositions with x = 0.00 and x = 0.03, **b** BFMO annealed at 550 °C for (I) 2 h, (II) 4 h, (III) 6 h **c** BFMO annealed for 2 h at (I) 500 °C, (II) 550 °C, (III) 600 °C

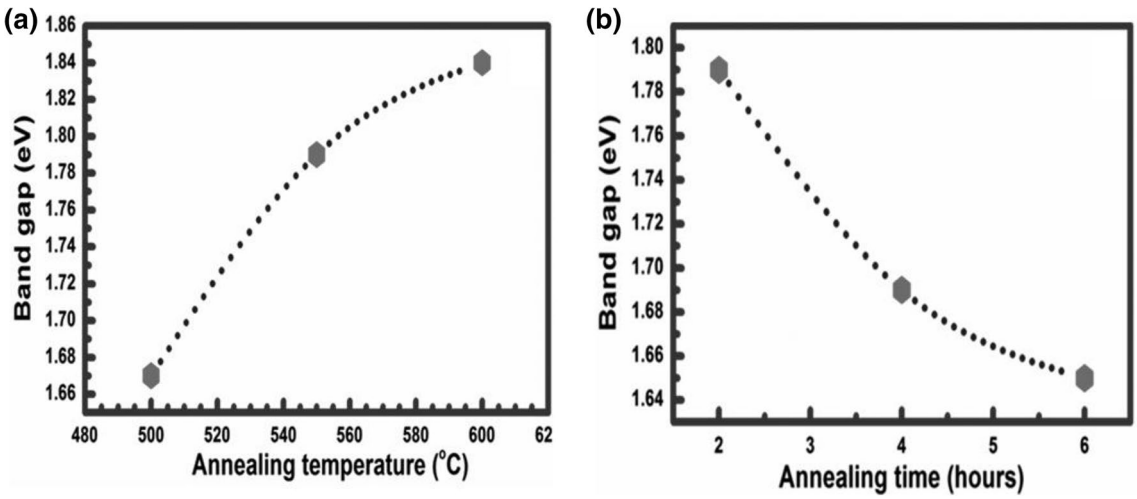

Fig. 12 Band-gap variation of BFMO samples as a function of **a** annealing temperature, **b** annealing time

However, our results show an increasing trend with an increase in annealing temperature, which is contrary to more commonly observed findings. As observed in XRD patterns of BFMO samples annealed at a different temperature, the samples annealed at 500 °C and 600 °C have shown more impurity peaks than the sample annealed at 550 °C; hence this contradiction may be attributed to the presence of impurity phases. However, a complete explanation is not yet there. In addition to this, BFMO sample, annealed at 550 °C can be considered as the lowest bandgap material without losing phase purity. The variation of bandgap values of BFMO as a function of annealing temperature and annealing time is shown in Figs. 12a, b, respectively. The observed results propose that the BFMO sample annealed at 550 °C for 2 h favours the highest light absorption without losing its purity, and hence promises to be a potential candidate for future photovoltaics.

4 Conclusions

In summary, a simple and cost-effective citrate precursor technique was employed to prepare undoped and Mn-doped BFO nanoparticles at the lowest known temperature (550 °C). Structural, morphological, and optical properties of BFO were found to vary with both Mn-doping as well as thermal annealing conditions. Mn-doped samples were subjected to various heat treatments and the perovskite structured BFO with the R3c group was confirmed by XRD studies. The average crystallite size was found to increase with the increase in annealing temperature and annealing time for both undoped BFO and Mn-doped BFO. FTIR spectral analysis confirmed the perovskite structure and structural distortion in BFMO. The optical bandgap was decreased significantly with Mn substitution. The bandgap values showed direct variation with annealing temperature and inverse variation with annealing time. The bandgap value of BFO was successfully tuned from 2.08–1.62 eV, which is suitable for light-harvesting applications for absorbing a broader spectrum of solar radiation. BFMO samples annealed at 550 °C for 2 h showed higher absorption coefficient and lower bandgap value without structural phase transition or additional phases in comparison to other samples prepared under different annealing conditions. The results obtained propose a user-friendly approach for synthesizing single-phase of BFO, and tailoring its optical bandgap via chemical substitution and varying thermal treatment conditions, which might be a promising tool for light-harvesting device applications. The citrate precursor method appears to be an attractive synthesis approach; however, careful control on thermal annealing conditions (annealing temperature, annealing time, heating rate) has a decisive impact on the phase formation, and other physical properties of BFO nanoceramics.

Acknowledgements We would like to thank DST-SERB(EMR/2017/002340) for supporting this project, and BITS Pilani, Hyderabad, for providing support and necessary infrastructure facilities. We also thank the Central Analytical Lab of BITS Pilani, Hyderabad, for providing all the characterization tools to make this work successfully in due time.

Authors contribution Waseem Ahmad Wani involved in conceptualization, methodology, investigation, writing—original draft and formal analysis. Souvik Kundu involved in writing—review and editing. Kannan Ramaswamy involved in writing—review and editing.

B. Harihara Venkataraman involved in writing—review and editing and supervision.

Compliance with ethical standards

Conflict of interest The authors declare that they have no known competing financial interests or personal relationships that could have appeared to influence the work reported in this paper.

Ethical standards The authors have complied with ethical guidelines, the work described has not been published previously, and it is not under consideration for publication elsewhere. Its publication is approved by all authors, and if accepted, it will not be published elsewhere without the written consent of the Publisher. Sincerely, Harihara Venkataraman (Corresponding author, on behalf of all the other authors).

References

1. Casper MD, Losego MD, Maria JP (2013) Optimizing phase and microstructure of chemical solution-deposited bismuth ferrite (BiFeO3) thin films to reduce DC leakage. J Mater Sci 48(4):1578–1584. https://doi.org/10.1007/s10853-012-6914-0
2. Ramesh R, Spaldin NA (2007) Multiferroics: progress and prospects in thin films. Nat Mater 6(1):21–29. https://doi.org/10.1038/nmat1805
3. Roy A, Gupta R, Garg A (2012) Multiferroic memories. Adv Condens Matter Phys. https://doi.org/10.1155/2012/926290
4. Irfan S, Zhuanghao Z, Li F, Chen YX, Liang GX, Luo JT, Ping F (2019) Critical review: Bismuth ferrite as an emerging visible light active nanostructured photocatalyst. J Mater Res Technol. https://doi.org/10.1016/j.jmrt.2019.10.004
5. Chauhan S, Kumar M, Chhoker S, Katyal SC, Singh H, Jewariya M, Yadav KL (2012) Multiferroic, magneto-electric and optical properties of Mn doped BiFeO3 nanoparticles. Solid State Commun 152(6):525–529. https://doi.org/10.1016/j.ssc.2011.12.037
6. Naganuma H, Miura J, Okamura S (2009) Annealing temperature effect on ferroelectric and magnetic properties in Mn-added polycrystalline BiFeO 3 films. J Electroceram 22(1–3):203–208. https://doi.org/10.1007/s10832-007-9400-3
7. Seshadri R, Hill NA (2001) Visualizing the role of Bi 6s "lone pairs" in the off-center distortion in ferromagnetic BiMnO3. Chem Mater 13(9):2892–2899. https://doi.org/10.1021/cm010090m
8. Mukherjee A, Hossain SM, Pal M, Basu S (2012) Effect of Y-doping on optical properties of multiferroics $BiFeO_3$ nanoparticles. Appl Nanosci 2(3):305–310. https://doi.org/10.1007/s13204-012-0114-8
9. Khomchenko VA, Troyanchuk IO, Kovetskaya MI, Kopcewicz M, Paixão JA (2012) Effect of Mn substitution on crystal structure and magnetic properties of $Bi_{1-x}Pr_xFeO_3$ multiferroics. J Phys D 45(4):045302. https://doi.org/10.1088/0022-3727/45/4/045302
10. Wu YJ, Zhang J, Chen XK, Chen XJ (2011) Phase evolution and magnetic property of Bi1−xHoxFeO3 powders. Solid State Commun 151(24):1936–1940. https://doi.org/10.1016/j.ssc.2011.09.020
11. HY Dai HZ Liu JF Du T Li RZ Xue ZP Chen 2014 Effect of Sintering Temperature on the Microstructure, Electrical, and Magnetic Properties of Bi0.85Eu0.15FeO3 Ceramics J Supercond Nov Magn 27 9 2105 2110 https://doi.org/10.1007/s10948-014-2558-4s
12. Kumar A, Varshney D (2012) Crystal structure refinement of $Bi_{1-x}Nd_xFeO_3$ multiferroic by the Rietveld method. Ceram Int 38(5):3935–3942. https://doi.org/10.1016/j.ceramint2012046
13. Irfan S, Shen Y, Rizwan S, Wang HC, Khan SB, Nan CW (2017) Band-gap engineering and enhanced photocatalytic activity of Sm and Mn doped BiFeO3 nanoparticles. J Am Ceram Soc 100(1):31–40. https://doi.org/10.1111/jace.14487
14. WA Wani S Kundu K Ramaswamy H Venkataraman 2020 Structural, morphological, optical and dielectric investigations in cobalt doped bismuth ferrite nanoceramics prepared using the sol-gel citrate precursor method J Alloys Compd 156334 https://doi.org/10.1016/j.jallcom.2020.156334
15. Naganuma H, Miura J, Okamura S (2008) Ferroelectric, electrical and magnetic properties of Cr, Mn Co, Ni, Cu added polycrystalline BiFeO3 films. Appl Phys Lett 93(5):052901. https://doi.org/10.1063/1.2965799
16. Zhu Y, Quan C, Ma Y, Wang Q, Mao W, Wang X, Huang W (2017) Effect of Eu, Mn co-doping on structural, optical and magnetic properties of BiFeO3 nanoparticles. Mater Sci Semicond Process 57:178–184. https://doi.org/10.1016/j.mssp.2016.10.023
17. Bernardo MS, Jardiel T, Peiteado M, Caballero AC, Villegas M (2011) Reaction pathways in the solid state synthesis of multiferroic $BiFeO_3$. J Eur Ceram Soc 31(16):3047–3053
18. Sagdeo A, Mondal P, Upadhyay A, Sinha AK, Srivastava AK, Gupta SM, Chowdhury P, Ganguli T, Deb SK (2013) Correlation of microstructural and physical properties in bulk $BiFeO_3$ prepared by rapid liquid-phase sintering. Solid State Sci 18:1–9. https://doi.org/10.1016/j.solidstatesciences.2012.12.017
19. Wani, W. A., Ramaswamy, K., Venkataraman, B. H., & Kundu, S. (2019, July). Influence of Transition Metal Ion Doping on Structural and Dielectric Properties of Sol-gel Synthesized Bismuth Ferrite Nanoceramics. In *2019 IEEE International Symposium on Applications of Ferroelectrics (ISAF)* (pp. 1–3). IEEE. https://doi.org/https://doi.org/10.1109/ISAF43169.2019.9034952
20. Yang X, Zhang Y, Xu G, Wei X, Ren Z, Shen G, Han G (2013) Phase and morphology evolution of bismuth ferrites via hydrothermal reaction route. Mater Res Bull 48(4):1694–1699. https://doi.org/10.1016/j.materresbull.2013.01.032
21. Abushad M, Khan W, Naseem S, Husain S, Nadeem M, Ansari A (2019) Influence of Mn doping on microstructure, optical, dielectric and magnetic properties of BiFeO3 nanoceramics synthesized via sol–gel method. Ceram Int 45(6):7437–7445. https://doi.org/10.1016/j.ceramint.2019.01.035
22. Chandel S, Thakur P, Tomar M, Gupta V, Thakur A (2017) Investigation of structural, optical, dielectric and magnetic studies of Mn substituted BiFeO3 multiferroics. Ceram Int 43(16):13750–13758. https://doi.org/10.1016/.j.ceramint.2017.07.088
23. Hua, H., Bao, G., Li, C., Zhu, Y., Yang, J., & Li, X. A. (2017). Effect of Ho, Mn co-doping on the structural, optical and ferroelectric properties of nanoparticles. *Journal of Materials Science: Materials in Electronics*, J. Mater. Sci. Mater. Electron. *28*(22), 17283–17287 https://doi.org/https://doi.org/10.1007/s10854-017-7660-5
24. Liu T, Xu Y, Feng S, Zhao J (2011) A facile route to the synthesis of BiFeO3 at low temperature. J Am Ceram Soc 94(9):3060–3063. https://doi.org/10.1111/j.1551-2916.2011.04536.x
25. Chen Z, Luo Z, Huang C, Qi Y, Yang P, You L, Hu C, Wu T, Wang J, Gao C, Sritharan T (2011) Low-symmetry monoclinic phases and polarization rotation path mediated by epitaxial strain in multiferroic $BiFeO_3$ thin films. Adv Funct Mater 21(1):133–138. https://doi.org/10.1002/adfm.201001867
26. Raj CA, Muneeswaran M, Jegatheesan P, Giridharan NV, Sivakumar V, Senguttuvan G (2013) Effect of annealing time in the low-temperature growth of BFO thin films spin coated on glass substrates. J Mater Sci Mater Electron 24(10):4148–4154. https://doi.org/10.1007/s10854-013-1374-0

27. Rong N, Chu M, Tang Y, Zhang C, Cui X, He H, Zhang Y, Xiao P (2016) Improved photoelectrocatalytic properties of Ti-doped $BiFeO_3$ films for water oxidation. J Mater Sci 51(12):5712–5723. https://doi.org/10.1007/s10853-016-9873-z
28. Gao F, Chen XY, Yin KB, Dong S, Ren ZF, Yuan F, Yu T, Zou ZG, Liu JM (2007) Visible-light photocatalytic properties of weak magnetic $BiFeO_3$ nanoparticles. Adv Mater 19(19):2889–2892. https://doi.org/10.1002/adma.200602377
29. Guo R, Fang L, Dong W, Zheng F, Shen M (2010) Enhanced photocatalytic activity and ferromagnetism in Gd doped $BiFeO_3$ nanoparticles. J Phys Chem C 114(49):21390–21396. https://doi.org/10.1021/jp104660a
30. Joshi UA, Jang JS, Borse PH, Lee JS (2008) Microwave synthesis of single-crystalline perovskite Bi Fe O3 nanocubes for photoelectrode and photocatalytic applications. Appl Phys Lett 92(24):242106. https://doi.org/10.1063/1.2946486
31. Rhaman MM, Matin MA, Hossain MN, Mozahid FA, Hakim MA, Islam MF (2019) Bandgap engineering of cobalt-doped bismuth ferrite nanoparticles for photovoltaic applications. Bull Mater Sci 42(4):190. https://doi.org/10.1007/s12034-019-1871-8
32. Lee JH, Ke X, Misra R, Ihlefeld JF, Xu XS, Mei ZG, Heeg T, Roeckerath M, Schubert J, Liu ZK, Musfeldt JL (2010) Adsorption-controlled growth of $BiMnO_3$ films by molecular-beam epitaxy. Appl Phys Lett 96(26):262905. https://doi.org/10.1063/1.3457786
33. Vishwakarma AK, Tripathi P, Srivastava A, Sinha AS, Srivastava ON (2017) Band gap engineering of Gd and Co doped $BiFeO_3$ and their application in hydrogen production through photoelectrochemical route. Int J Hydrog Energy 42(36):22677–22686. https://doi.org/10.1016/j.ijhydene.2017.07.153
34. Sati PC, Arora M, Chauhan S, Kumar M, Chhoker S (2014) Effect of Dy substitution on structural, magnetic and optical properties of BiFeO3 ceramics. J Phys Chem Solids 75(1):105–108. https://doi.org/10.1016/j.jpcs.2013.09.003
35. Lin H, Huang CP, Li W, Ni C, Shah SI, Tseng YH (2006) Size dependency of nanocrystalline TiO2 on its optical property and photocatalytic reactivity exemplified by 2-chlorophenol. Appl Catal B 68(1–2):1–11. https://doi.org/10.1016/j.apcatb.2006.07.018
36. Mocherla PS, Karthik C, Ubic R, Ramachandra Rao MS, Sudakar C (2013) Tunable bandgap in $BiFeO_3$ nanoparticles: the role of microstrain and oxygen defects. Appl Phys Lett 103(2):022910. https://doi.org/10.1063/1.4813539
37. Gómez-Salces S, Aguado F, Rodríguez F, Valiente R, González J, Haumont R, Kreisel J (2012) Effect of pressure on the band gap and the local FeO_6 environment in $BiFeO_3$. Phys Rev B 85(14):144109. https://doi.org/10.1103/PhysRevB.85.144109
38. Song MG, Han JY, Bark CW (2015) The effect of annealing temperature on the bandgap of $Bi_{3.25}La_{0.75}FeTi_2O_{12}$ powders. J Nanosci Nanotechnol 15(10):8195–8198. https://doi.org/10.1166/jnn.2015.11275
39. Irshad Z, Shah SH, Rafiq MA, Hasan MM (2015) First principles study of structural, electronic and magnetic properties of ferromagnetic $Bi_2Fe_4O_9$. J Alloys Compd 624:131–136. https://doi.org/10.1016/j.jallcom.2014.10.174